Received 8 October 2021; revised 17 November 2021; accepted 20 November 2021. Date of publication 25 November 2021; date of current version 3 December 2021.

*Digital Object Identifier 10.1109/OJCOMS.2021.3130757*

# Frequency-Domain SWIPT and Modulation Classification: Design and Experimental Validation

**RAHUL GUPTA, KONSTANTINOS NTOUGIAS (Member, IEEE), AND IOANNIS KRIKIDIS (Fellow, IEEE)**

Department of Electrical and Computer Engineering, University of Cyprus, 1070 Nicosia, Cyprus

CORRESPONDING AUTHOR: K. NTOUGIAS (e-mail: ntougias.konstantinos@ucy.ac.cy)

This work was supported in part by the European Regional Development Fund and the Republic of Cyprus through the Research and Innovation Foundation under Project INFRASTRUCTURES/1216/0017 (IRIDA) and Project EXCELLENCE/1918/0377 (PRIME), and in part by the European Research Council (ERC) through the EU's Horizon 2020 Research and Innovation Programme under Grant 819819.

**ABSTRACT** Simultaneous wireless information and power transfer (SWIPT) constitutes an emerging paradigm that prolongs the lifetime of energy-constrained devices, such as wireless sensors and Internet-of-Things (IoT) nodes. Its frequency-domain (FD) variant enables energy harvesting (EH) by using (low-power) local oscillators/mixers. In this paper, a novel FD-SWIPT waveform design that minimizes the multitone interference induced to the information signal by the energy signal, thus eliminating the need for using receive filters to this end, is described. The inherent interference suppression of the proposed strategy allows also for applying modulation classification (MC). This functionality is highly desirable in contemporary networks, where the access points utilize adaptive transmission. In this context, we analytically derive the average error probability of the proposed waveform over a Rayleigh fading channel for various modulation schemes under non-zero interference and frequency synchronization errors. Furthermore, we optimize the power of the energy tones, such that the signal-to-interference-ratio at the information signal is maximized subject to the EH and transmission power constraints. In addition, we investigate the coexistence of SWIPT with blind MC under this framework. Numerical simulation results reveal that the proposed approach substantially increases both the data rate and the harvested power in comparison to the conventional power-splitting method at the cost of a negligibly higher error probability. Also, they indicate that the employed MC scheme achieves a high success rate even in the low signal-to-noise-ratio regime. The proposed concept is validated experimentally in a realistic indoor environment by using a testbed based on software-defined radio units.

**INDEX TERMS** SWIPT, multitone energy signal, waveform design, optimization, experimental validation.

## I. INTRODUCTION

FIFTH generation (5G) networks are characterized by the proliferation of battery-powered terminals with small energy storage capacity, such as wireless sensors and Internet-of-Things (IoT) nodes [1], [2]. Consequently, the realization of energy-sustainable operation is regarded as a matter of utmost importance by the community, since the massive volume of these energy-constrained devices renders the wired charging or replacement of their batteries a cumbersome and costly task. Specifically, there is a growing interest in the development of techniques that concurrently utilize the transmitted radio frequency (RF) waves for both information and power transfer (IT/PT) purposes. Then, we can replenish the stored energy at the end devices via energy harvesting (EH) [3], [4].

The receivers that support the aforementioned simultaneous wireless information and power transfer (SWIPT) paradigm are comprised by an information decoding (ID) module and an EH one. The former performs data detection at the baseband, whereas the latter transforms the received RF power into direct current (DC) power, which is suitable for battery charging [5]. The main practical SWIPT receiver

architectures are: i) time switching (TS), wherein a switch connects the receive antenna(s) to the ID and EH units at different times; and ii) power splitting (PS), where the received RF power is split among two streams that are directed to the ID and EH circuits, respectively [5]. The major drawback of such orthogonal demultiplexing approaches is that they *underutilize the available resources*.

The EH module is typically implemented as a rectifier, which consists of one or more diodes interconnected in some topology (e.g., half-wave rectifier, single-stage voltage multiplier, etc.), followed by a low-pass filter (LPF) [6]. The amount of harvested energy is determined by the RF-to-DC energy conversion efficiency, which depends on the implementation of the EH circuit [6] and the input waveform (power and shape) [7]. The non-linear relationship of the RF-to-DC energy conversion efficiency with the input waveform under a diodes-based EH circuit implementation triggered a number of studies on the characterization of these non-linearities and the design of efficient SWIPT waveforms that maximize the harvested power for a given transmit power, along with relevant prototyping and experimental validation activities [8], [9], [10]. These research works revealed that the rectifier's non-linearity is beneficial in terms of EH efficiency, provided that it is exploited in the design of SWIPT waveforms.

5G networks are highly complex and dynamic systems. For instance, the access points commonly employ adaptive transmission techniques to enhance the performance under the variability of the wireless channel. In this context, they freely choose, among other things, the applied modulation scheme in each transmission slot, typically based on link quality. However, the knowledge of the modulation type at the receiver is a prerequisite for effective demodulation. The use of blind modulation classification (MC) methods solves this problem in a spectrally efficient way, since it avoids the transmission of training sequences/pilot symbols for modulation identification purposes [11]. Blind MC schemes are divided into likelihood-based (LB) and feature-based (FB). The former methods perform better, but they suffer from high computational complexity and require the sharing of side information (e.g., carrier frequency) [12]. FB methods, on the other hand, are low-complexity techniques that do not require prior information [13], [14], [15].

### A. MOTIVATION AND RELATED WORK

Frequency-domain (FD) SWIPT represents an alternative to TS-/PS-SWIPT, which is based on the separation of the IT and PT waveforms in the frequency domain and the *direct* extraction of the corresponding streams at the receiver using appropriate filters, thus *enhancing the utilization efficiency of the available resources*. Moreover, certain designs leverage sufficient IT/PT signal separation at the frequency domain to avoid the use of a diodes-based rectifier, which *constitutes an additional hardware component that increases the cost and size of the device*; they rely instead on direct down-conversion achieved via local oscillators (LO) that operate in the frequency of the PT signal's tones. This approach is motivated by the fact that contemporary wireless sensors/IoT nodes are typically equipped already with **ultra-low-power** LOs/mixers for data detection purposes that consume only around 120–520 microwatts [16], [17], [18], which is within the harvested RF energy range.

In [19] and [20], the DC sub-carrier of an orthogonal frequency division multiplexing (OFDM) IT signal is used as a PT signal. In the former study, the receiver extracts the DC PT signal using a local oscillator operating at the carrier frequency and a DC LPF. The latter work, on the other hand, proposes a frequency-splitting (FS) receiver architecture that makes use of a three-port circulator and a notch filter to separate the PT and IT signals. The utilization of a conventional diodes-based rectifier is assumed in this case. The authors showed that the proposed scheme outperforms PS-SWIPT in the presence of high power amplifier (HPA) non-linearities. Another type of FD-SWIPT waveform, which is based on superimposing a continuous-phase modulation (CPM) IT signal and a multitone PT signal, is described in [21]. The use of the latter is dictated by spectral regulations, which might prevent the transmission of a single high-power tone as in [19], [20]. Furthermore, multitone energy signals are easy to generate and they significantly boost the average harvested power when a non-linear rectifier circuit is utilized for RF-to-DC energy conversion purposes, as it has been shown by experimental works [22]. In this study, the authors use a combination of peak and notch filters to separate the PT and IT signals, respectively, over an additive white Gaussian noise (AWGN) channel. The PT components are placed at the spectral nulls or/and low-power sub-bands of the CPM signal to minimize the interference induced to the IT signal and reduce the attenuation of that signal caused by the non-ideal characteristics of practical filters (i.e., energy leakage). This design is compatible with both types of EH circuit implementations, i.e., diodes-based rectifier and local oscillators-based down-converter, thus providing greater flexibility. The downside of these FD-SWIPT techniques is that they require the utilization of additional filters at the receiver for IT/PT signal separation, thus increasing the cost.

The application of FB-MC schemes in wireless communication systems has been studied manifold in the literature. These works introduced algorithms that extract instantaneous features (amplitude, frequency, phase) [23]; transformation-based features via Fourier and wavelet transforms [24]; statistical features by using high-order cumulants [25]; cyclostationary features [26], etc. Nevertheless, the coexistence of MC with EH in SWIPT systems in general and FD-SWIPT setups in particular under the potential interference induced to the information streams by wireless power supply has not been investigated yet, to the best of the authors' knowledge.

### B. CONTRIBUTIONS

In this work we propose a novel FD-SWIPT approach, where waveform design is based on the frequency domain multiplexing of a modulation signal with a multitone PT

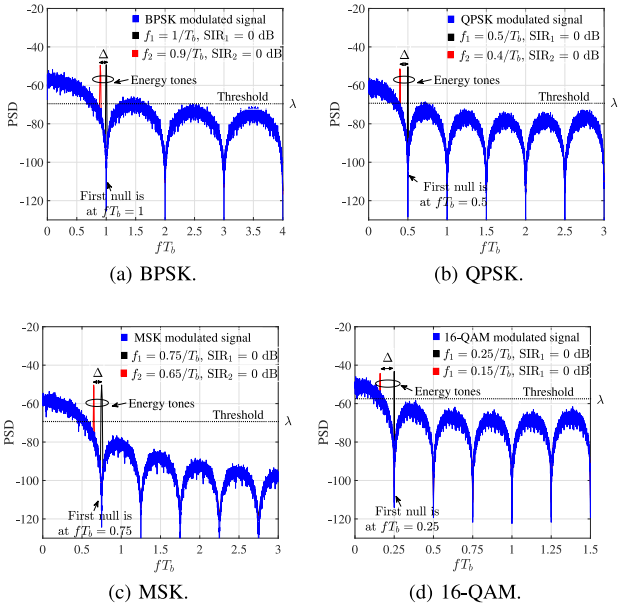


(a) BPSK. (b) QPSK. (c) MSK. (d) 16-QAM.

**FIGURE 1.** Power spectral density of the proposed FD-SWIPT waveforms, where different modulated information signals are superimposed with a two-tones energy signal.

signal. The considered framework consists of placing the frequency components of the PT signal at the spectral nulls and/or low-power sub-bands that characterize the power spectral density (PSD) of the IT signal, so that the resulting multitone interference is minimized. In contrast to prior studies, though, we argue that sufficient separability of the IT and PT signals in the frequency domain can avoid the use of expensive, yet non-ideal notch/peak filters altogether. Under this context, we investigate the performance of the proposed FD-SWIPT design for various modulation schemes in the absence of receive filters. Therefore, we consider in the analytical studies and numerical simulations the, low under proper waveform design as mentioned earlier but non-zero nevertheless, multitone interference. Also, for the analytical characterization of the probability of error to have practical value, we take into account the frequency synchronization errors that are typically observed in actual implementations and quantify their performance impact. This commonly occurring phenomenon, which is often neglected in relevant studies, is mainly attributed to a mismatch in the frequency of the oscillators at the transmitter and the receiver as well as to Doppler shifts [27] and it significantly affects the error rate performance.

An example of the proposed FD-SWIPT waveforms for different modulations–namely, binary phase shift keying (BPSK), quadrature PSK (QPSK), minimum shift keying (MSK), and 16-quadrature amplitude modulation (16-QAM)–, is illustrated in Fig. 1. In this case, we consider a PT signal with $N = 2$ tones $f_i$ $(i = 1, \ldots, N)$ that are placed in the low-power sub-bands of the modulation signal. For MSK signals, the locations of the energy tones are $0.75/T_b$ and $0.65/T_b$, with the first frequency null at $fT_b = 0.75$, where $T_b$ is the bit duration. The normalized tone spacing is $\Delta = 0.1$ and $\lambda$ denotes the threshold that defines the low-power sub-band. The latter is considered in the design of the PT waveform in Section IV-B.

We should mention that the proposed design approach supports RF-to-DC energy conversion via a bank of ultra-low-power LOs and mixers, in line with the stringent cost, energy consumption, and size constraints of wireless sensors and IoT terminals. This fact justifies the consideration of conventional modulation schemes, since there are no diodes-based non-linearities to exploit in this case. Nonetheless, the proposed scheme provides the flexibility of using commercial-off-the-shelf (COTS) devices that adopt a diodes-based rectifier (and a PS receiver architecture, for that matter) for EH purposes as well. In this scenario, the utilization of the multitone PT signal is beneficial, in terms of EH efficiency.

The integration of the SWIPT and blind MC concepts constitutes a promising approach for realizing energy-autonomous and radio-aware wireless communication systems that are able to respond to the constantly increasing demands for efficient connectivity [28]. For instance, MC functionality could facilitate data detection or foster the monitoring of interfering signals. Within this context, we study the coexistence of the proposed FD-SWIPT design framework with FB-MC under the minimized, yet non-zero multitone interference induced to the IT signal. The use of blind MC in the context of FD-SWIPT receivers, and especially under multitone interference, has not been previously investigated, to the best of our knowledge.

Numerical simulations highlight the substantial performance gains of the proposed FD-SWIPT scheme, in terms of the achieved data rate and harvested power, against conventional PS-SWIPT architectures. Furthermore, the simulation results indicate that the resulting detection performance loss is negligible, as well as that the success rate of MC is high even in the low signal-to-noise-ratio (SNR) regime.

The unique contributions of this paper that set it apart from similar studies, such as the work in [21], are listed below:

- We analytically derive the average error probability for various proposed FD-SWIPT waveforms, assuming a point-to-point Rayleigh fading channel, in the presence of *multitone interference* and considering a system with or without *frequency synchronization errors*, respectively.
- We *optimize the power of the energy signal's tones* such that the signal-to-interference-ratio (SIR) of the IT signal is maximized under the EH and tones' power constraints.
- We apply an FB-MC scheme that exploits the location of the PT tones and study its integration in the FD-SWIPT receiver. Feature-extraction is based on the discrete Fourier transform (DFT) of the absolute value of the discrete low-pass received signal.

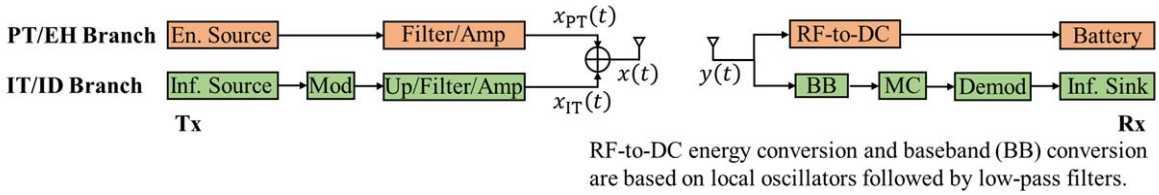


**FIGURE 2.** Block diagram of the proposed FD-SWIPT transmitter (Tx) and receiver (Rx).

- The proposed concept is experimentally validated via measurements performed in a realistic indoor propagation environment by using a software-defined radio (SDR)-based testbed and COTS powercast modules.
- We evaluate the performance of the proposed FD-SWIPT method via numerical simulation studies. We consider either an *LOs-based receiver without notch/peak filters* or a *PS-based one*, for comparison purposes. We also consider the, widely adopted in the literature, piecewise linear and sigmoidal EH models in the latter scenario to capture the non-linear behavior of the diodes-based rectifier circuit. Numerical results reveal the impact of various parameters on system's performance and highlight the performance gains of the proposed design.

This paper is structured as follows: Section II introduces the system model as well as the considered non-linear EH models and performance metrics. Section III focuses on the error rate analysis of the proposed FD-SWIPT waveforms. Section IV presents the blind MC algorithm and the optimization of the multitone energy signal. Section V describes the experimental validation and presents the numerical simulation results. Finally, Section VI provides our conclusions. The mathematical proofs are given in Appendices.

## II. FD-SWIPT SYSTEM MODEL

### A. TRANSMITTER

The block diagram of the proposed FD-SWIPT transmitter is depicted in Fig. 2. At the transmitter, information is modulated using a conventional modulation scheme and then the modulated signal is up-converted. Also, a multitone energy signal is generated, with a controllable frequency and amplitude for each tone. The modulated data signal and the multitone energy signal are filtered, amplified, and combined; then, the composite signal is transmitted.

Hence, the transmitted FD-SWIPT signal $x(t)$ can be expressed as

$$x(t) = x_{\mathrm{IT}}(t) + x_{\mathrm{PT}}(t), \tag{1}$$

where $x_{\mathrm{IT}}(t)$ denotes the modulated IT signal and $x_{\mathrm{PT}}(t)$ represents the multitone PT signal. The latter signal can be written as

$$x_{\mathrm{PT}}(t) = \sum_{i=1}^{N} \alpha_i \cos(w_c t + w_i t + \theta_i), \tag{2}$$

where $\alpha_i$ and $w_i$ denote the $i$-th tone's amplitude and angular frequency, respectively ($i = 1, \ldots, N$; $w_i = 2\pi f_i$), which are design parameters of the PT signal; $w_c$ refers to the angular carrier frequency ($w_c = 2\pi f_c$); $N$ represents the number of tones; and $\theta_i$ denotes the phases, which are arbitrary. We define the SIR of the IT signal for the $i$-th tone as $\mathrm{SIR}_i = S^2/\alpha_i^2$, where $S$ denotes the amplitude of the carrier signal. The modulated IT signal for the various modulation schemes is defined next.

#### 1) BPSK SIGNAL

The BPSK modulated information signal is defined in terms of orthonormal basis functions $\phi_b(t)$ as

$$x_{\mathrm{IT}_b}(t) = s_b \phi_b(t), \tag{3}$$

where $\phi_b(t) = \sqrt{\frac{2}{T_b}}\cos(w_c t), 0 \le t \le T_b$, and $s_b = \pm\sqrt{E_b}$ refers to the coordinates of the message points, $E_b$ denotes the bit energy and $T_b$ is the bit duration. The PSD of the BPSK modulated signal is expressed as [29]

$$S(f) = 2E_b\left[\frac{\sin(\pi f T_b)}{\pi f T_b}\right]^2. \tag{4}$$

From eq. (4), we can compute the spectral null frequencies of the BPSK modulated signal as

$$S(f) = 2E_b\left[\frac{\sin(\pi f T_b)}{\pi f T_b}\right]^2 = 0 \Rightarrow f T_b = n, \tag{5}$$

where $n$ is integer and the first null is at $n = 1$, i.e., $fT_b = 1$ as shown in Fig. 1a.

#### 2) QPSK SIGNAL

The QPSK modulated information signal is defined in terms of orthonormal basis functions $\phi_{q_1}(t)$ and $\phi_{q_2}(t)$ as [29]

$$x_{\mathrm{IT}_q}(t) = s_{q_1}\phi_{q_1}(t) + s_{q_2}\phi_{q_2}(t), \tag{6}$$

where

$$2\phi_{q_1}(t) = \sqrt{\frac{2}{T_s}}\cos(w_c t), \qquad 0 \le t \le T_s, \tag{7a}$$

$$\phi_{q_2}(t) = \sqrt{\frac{2}{T_s}}\sin(w_c t), \qquad 0 \le t \le T_s. \tag{7b}$$

In eq. (6), the tuple $(s_{q_1}, s_{q_2}) = (\pm\sqrt{E_s}, \pm\sqrt{E_s})$ refers to the coordinates of the message points, where $E_s = 2E_b$ denotes

the symbol energy and $T_s = 2T_b$ is the symbol duration. The PSD of the QPSK modulated signal is expressed as [29]

$$S(f) = 4E_b\left[\frac{\sin(2\pi fT_b)}{2\pi fT_b}\right]^2. \tag{8}$$

Thus, the spectral null frequencies of the QPSK modulated signal are obtained as

$$S(f) = 4E_b\left[\frac{\sin(2\pi fT_b)}{2\pi fT_b}\right]^2 = 0 \Rightarrow fT_b = n/2, \tag{9}$$

where the first null is at $n = 1$, i.e., $fT_b = 0.5$ as shown in Fig. 1b.

#### 3) MSK SIGNAL

The MSK modulated information signal is defined in terms of orthonormal basis functions $\phi_{m_1}(t)$ and $\phi_{m_2}(t)$ as [30]

$$x_{\mathrm{IT}_m}(t) = s_{m_1}\phi_{m_1}(t) + s_{m_2}\phi_{m_2}(t), \tag{10}$$

where

$$\phi_{m_1}(t) = \sqrt{\frac{2}{T_b}}\cos\left(\frac{\pi t}{2T_b}\right)\cos(w_c t), \quad -T_b \le t \le T_b, \tag{11a}$$

$$\phi_{m_2}(t) = \sqrt{\frac{2}{T_b}}\sin\left(\frac{\pi t}{2T_b}\right)\sin(w_c t), \quad 0 \le t \le 2T_b. \tag{11b}$$

In eq. (10), the tuple $(s_{m_1}, s_{m_2}) = (\pm\sqrt{E_b}, \pm\sqrt{E_b})$ refers to the coordinates of the message points. The PSD of the MSK modulated signal is expressed as [31]

$$S(f) = \frac{32E_b}{\pi^2}\left[\frac{\cos(2\pi fT_b)}{1-(4fT_b)^2}\right]^2. \tag{12}$$

Thus, we can compute the spectral null frequencies of the MSK modulated signal as follows:

$$S(f) = \frac{32E_b}{\pi^2}\left[\frac{\cos(2\pi fT_b)}{1-(4fT_b)^2}\right]^2 = 0 \Rightarrow fT_b = \frac{2n+1}{4}, \tag{13}$$

where the first null is at $n = 1$, i.e., $fT_b = 0.75$ as shown in Fig. 1c.

#### 4) 16-QAM SIGNAL

The 16-QAM modulated information signal is defined in terms of orthonormal basis functions $\phi_{q_1}(t)$ and $\phi_{q_2}(t)$ as [29]

$$x_{\mathrm{IT}_{\bar{q}}}(t) = s_{\bar{q}_1}\phi_{q_1}(t) + s_{\bar{q}_2}\phi_{q_2}(t), \tag{14}$$

where $s_{\bar{q}_1}, s_{\bar{q}_2} \in \{\pm\sqrt{E_s}/\sqrt{10}, \pm 3\sqrt{E_s}/\sqrt{10}\}$ refer to the coordinates of the message points, $T_s = 4T_b$ and $E_s = 4E_b$. The PSD of the 16-QAM modulated signal is expressed as [29]

$$S(f) = 8E_b\left[\frac{\sin(4\pi fT_b)}{4\pi fT_b}\right]^2. \tag{15}$$

Thus, the first null of the 16-QAM modulated signal is at $fT_b = 0.25$ as shown in Fig. 1d.

### B. RECEIVER

The block diagram of the proposed FD-SWIPT receiver is shown in Fig. 2. By assuming a transmission over an independent and identically distributed (i.i.d.) Rayleigh block fading channel with AWGN, the received baseband equivalent signal is given by

$$y(t) = hx(t) + n(t), \tag{16}$$

where $h$ denotes the i.i.d. zero-mean complex Gaussian channel impulse response with a unit variance and $n(t)$ represents the AWGN with a variance $N_0$.

As illustrated in Fig. 2, in the EH branch the received signal $y(t)$ is forwarded to the RF-to-DC energy conversion circuit, which is based on a bank of local oscillators that operate in the frequencies of the energy tones followed by an LPF, thus translating the PT signal's tones to DC. Then, the DC power at the output charges the battery. Similarly, in the ID branch, the received signal is converted to baseband with the assistance of a local oscillator operating at the carrier frequency. Next, it is passed through the MC circuit and the demodulator. The decoded data are finally send to the information sink. Notice that baseband conversion in the ID branch for data detection purposes gives rise to additional i.i.d. zero-mean complex Gaussian circuit noise $n_c(t)$ with a variance $N_c$.

The RF-to-DC energy conversion circuit employs direct down-conversion of the PT signal's tones by using the, already in place for data detection purposes, ultra-low-power LOs and mixers of the receiver, as described earlier. Therefore, it reduces the complexity, cost, and size of the EH circuit in comparison to a diodes-based rectifier implementation. However, the proposed FD-SWIPT waveform supports also diodes-based rectifier or/and PS-SWIPT receiver architectures as well, as already mentioned. Such compatibility facilitates its practical application with currently available COTS hardware and, therefore, accelerates its potential adoption by standards.

This concept is similar to the FD-SWIPT design in [21], as stated in Section II-B of this cited work: "The EH can be formed by using a rectifier [$\cdots$]. Another alternative is to use direct down conversion at frequencies used for the PT signal." and again in Section IV-B: "The EH module for CPM-SWIPT can be implemented without diodes, by using the RF-to-DC conversion of the PT tones, through local oscillators operating at the tone frequencies." However, in our approach, no notch filters are required in the ID branch, in contrast to [21], since with proper waveform design the multitone interference is negligible and does not essentially degrade the data detection performance, as we shall see in the subsequent sections.

When a conventional PS-based receiver is utilized [32], [33], a portion $\rho$ of the received signal's power is allocated to the EH branch and the remaining portion $(1-\rho)$ is allocated to the ID branch, where $0 < \rho < 1$ is the PS factor. Thus, the received signal at the input of the RF-to-DC energy conversion unit (which might be a diodes-based

rectifier) in the EH branch and the demodulator in the ID branch (i.e., after baseband conversion) in this case is given, respectively, by

$$y_{\mathrm{PT}}(t) = \sqrt{\rho}y(t),\ \ y_{\mathrm{IT}}(t) = \sqrt{(1-\rho)}y(t) + n_c(t). \quad (17)$$

### C. HARVESTED ENERGY

The instantaneous power of the received RF signal, ignoring the negligible AWGN power, is given by

$$P_r = |y(t)|^2 = |h|^2 P, \quad (18)$$

where $P$ is the transmit power.

When a local oscillators-based receiver is utilized, the harvested DC power is given by

$$P_{\mathrm{DC}} = |hx_{\mathrm{PT}}(t)|^2 = |h|^2 \sum_{i=1}^{N} \alpha_i^2. \quad (19)$$

When a PS-SWIPT receiver with a diodes-based rectifier is used, on the other hand, the instantaneous power at the input of the RF-to-DC energy conversion unit is $P_{\mathrm{EH}} = \rho P_r$. We consider two well-known EH models that capture the non-linear behavior of the rectifying diodes, namely, the piecewise linear and the sigmoidal models. Under the former model, which is widely adopted due to its mathematical tractability, the harvested DC power at the output of the EH circuit can be written as [33], [34]

$$P_{\mathrm{DC}} = \begin{cases} 0, & \rho P_r < P_{\mathrm{th}_1}; \\ \eta\left(\rho P_r - P_{\mathrm{th}_1}\right), & P_{\mathrm{th}_1} \le \rho P_r \le P_{\mathrm{th}_2}; \\ \eta P_{\mathrm{th}_2}, & \rho P_r > P_{\mathrm{th}_2}, \end{cases} \quad (20)$$

where $0 < \eta < 1$ represents the RF-to-DC conversion efficiency, while $P_{\mathrm{th}_1}$ and $P_{\mathrm{th}_2}$ denote the sensitivity and saturation thresholds of the rectifier circuit, respectively.

Under the non-linear sigmoidal model, in turn, the harvested DC power is given by [34], [35]

$$P_{\mathrm{DC}} = \frac{P_{\mathrm{th}_2}(\Omega_r - \Omega)}{1-\Omega}, \quad (21a)$$

$$\Omega_r = \frac{1}{1+e^{-a_1(\rho P_r - a_2)}},\ \ \Omega = \frac{1}{1+e^{a_1 a_2}}, \quad (21b)$$

where the parameters $a_1$ and $a_2$ are constants related to the specifications of the EH circuit.

Equations (20) and (21) reveal the negative impact of the power splitting ratio $\rho$ and the energy conversion efficiency factor $\eta$ on the harvested DC power in PS-SWIPT receivers with diodes-based rectifiers. The different expressions of the harvested DC power according to the applied EH method and model are summarized in Table 1.

### D. ERGODIC CAPACITY

The instantaneous power of the received signal (neglecting AWGN) at the ID branch of the local oscillators-based receiver, $P_{\mathrm{r,LO}}$, and the PS-based receiver, $P_{\mathrm{r,PS}}$, is given by

$$P_{\mathrm{r,LO}} = |h|^2 \sum_{i=1}^{N} \alpha_i^2,\ \ P_{\mathrm{r,PS}} = (1-\rho)|h|^2 P. \quad (22)$$

**TABLE 1.** Harvested power expressions for different EH methods and models.

| EH MODEL | HARVESTED POWER |
|---|---|
| Local Oscillators | $P_{\mathrm{DC}} = \lvert h\rvert^2 \sum_{i=1}^{N} \alpha_i^2$. |
| Piecewise | $P_{\mathrm{DC}} = \begin{cases} 0, & P_{\mathrm{EH}} < P_{\mathrm{th}_1}; \\ \eta\left(P_{\mathrm{EH}} - P_{\mathrm{th}_1}\right), & P_{\mathrm{th}_1} \le P_{\mathrm{EH}} \le P_{\mathrm{th}_2}; \\ \eta P_{\mathrm{th}_2}, & P_{\mathrm{EH}} > P_{\mathrm{th}_2}. \end{cases}$ |
| Logistic (sigmoidal) | $P_{\mathrm{DC}} = \frac{P_{\mathrm{th}_2}(\Omega_r - \Omega)}{1-\Omega}$. |
| Notes: | $P_{\mathrm{EH}} = \rho P_r = \rho \lvert h\rvert^2 P$; $\Omega_r = \frac{1}{1+e^{-a_1(P_{\mathrm{EH}} - a_2)}}$; $\Omega = \frac{1}{1+e^{a_1 a_2}}$. |

Thus, the instantaneous receive SNR is expressed as

$$\mathrm{SNR}_{\mathrm{LO}} = \frac{|h|^2 \sum_{i=1}^{N} \alpha_i^2}{N_0 + N_c},\ \ \mathrm{SNR}_{\mathrm{PS}} = \frac{|h|^2 P}{N_0 + \frac{N_c}{(1-\rho)}}. \quad (23)$$

The ergodic capacity is given by $R_{\mathrm{x}} = \mathbb{E}\{\log_2(1+\mathrm{SNR}_{\mathrm{x}})\}$, with $\mathrm{x} \in \{\mathrm{LO}, \mathrm{PS}\}$. In eq. (23), we note the negative impact of the power splitting ratio $\rho$ on the SNR and, therefore, on the ergodic capacity of PS-SWIPT systems.

## III. ERROR RATE ANALYSIS

In this section, we evaluate the overall average error probability of the proposed FD-SWIPT system for various modulation schemes over a Rayleigh fading channel, by considering the presence of multitone interference and frequency synchronization errors.

### A. BPSK

The BPSK demodulation is implemented via a correlator receiver. By assuming initially an AWGN channel with a frequency synchronization error ($w_o = 2\pi f_o$), the integrator output at the ID circuit in the presence of multitone interference is expressed as

$$r = \int_0^{T_b} \sqrt{\frac{2}{T_b}} \cos(w_c t + w_o t) \times \left[x_{\mathrm{IT}_b}(t) + x_{\mathrm{PT}}(t) + n(t)\right] dt. \quad (24)$$

After simplifying the above integral (see Appendix A), we obtain

$$r = \sqrt{E_b}(A + B) + N_0, \quad (25)$$

where

$$A = \frac{\sin(2\pi f_o T_b)}{2\pi f_o T_b} \quad \text{and}$$

$$B = \sum_{i=1}^{N} \frac{\sin\left[2\pi(f_i - f_o)T_b + \theta_i\right] - \sin\theta_i}{\sqrt{\mathrm{SIR}_i}\ 2\pi(f_i - f_o)T_b}.$$

Then, the probability of error is given by

$$P_e = \frac{1}{2}\mathrm{erfc}\left[\sqrt{\mathrm{SNR}}(A+B)\right], \quad (26)$$

where $\mathrm{SNR} = E_b/N_0 = S^2 T_b/2N_0$ and the complementary error function $\mathrm{erfc}(\cdot)$ is defined as $\mathrm{erfc}(x) \triangleq \frac{2}{\sqrt{\pi}} \int_x^{\infty} e^{-t^2} dt$.

Next, we compute the error probability in the presence of a standard (i.e., normalized) i.i.d. Rayleigh fading. Under this context, the probability density function (PDF) of $h$ is given by $f_{\mathcal{H}}(h) = 2he^{-h^2}$. Hence, the PDF of fading power $b = |h|^2$ is equal to $f_{\mathcal{B}}(b) = e^{-b}$. From eq. (26), we can compute the average error probability over a Rayleigh fading as

$$P_{avg} = \int_0^{\infty} \frac{1}{2}\text{erfc}\Big[\sqrt{b}\sqrt{\text{SNR}}(A+B)\Big]e^{-b}db. \quad (27)$$

After solving the above integral (see Appendix A), we obtain the overall average error probability over a Rayleigh fading channel as

$$P_{avg} = \frac{1}{2}\left[1 - \sqrt{\frac{\Gamma}{\Gamma+1}}\right], \quad (28)$$

where $\Gamma = \text{SNR}(A+B)^2$. At high SNRs, the overall asymptotic average error probability is approximately given as $P_{avg} \approx \frac{1}{4\Gamma}$.

*Special Case I:* In the ideal case where $f_o = 0$, the overall average error probability is given by replacing $\Gamma$ with $\Gamma_0$ in eq. (28), where $\Gamma_0 = \text{SNR}(1 + \sum_{i=1}^{N} \frac{\sin[2\pi f_i T_b + \theta_i] - \sin\theta_i}{\sqrt{\text{SIR}_i}\ 2\pi f_i T_b})^2$.

### B. QPSK

The QPSK demodulation is implemented via a conventional I/Q architecture, where I and Q stand for the in-phase and quadrature branches, respectively. By using the same approach as in the BPSK case, we express the integrator output at the ID circuit for the I-branch as

$$r_I = \int_0^{T_s} \sqrt{\frac{2}{T_s}}\cos(w_c t + w_o t) \times \Big[x_{\text{IT}_q}(t) + x_{\text{PT}}(t) + n(t)\Big]dt. \quad (29)$$

After simplifying the above integral (see Appendix B), we have

$$r = \sqrt{E_s}(A_I + B_I) + N_0, \quad (30)$$

where

$$A_I = \frac{\sin(2\pi f_o T_s) + \cos(2\pi f_o T_s) - 1}{2\pi f_o T_s}, \text{ and}$$

$$B_I = \sum_{i=1}^{N} \frac{\sin[2\pi(f_i - f_o)T_s + \theta_i] - \sin\theta_i}{\sqrt{\text{SIR}_i}\ 2\pi(f_i - f_o)T_s}.$$

Then, the probability of error for the I-branch is obtained as

$$P_{e_I} = \frac{1}{2}\text{erfc}\Big[\sqrt{\text{SNR}}(A_I + B_I)\Big]. \quad (31)$$

Similarly, the integrator output for the Q-branch is given by

$$r_Q = \int_0^{T_s} \sqrt{\frac{2}{T_s}}\sin(w_c t + w_o t) \times \Big[x_{\text{IT}_q}(t) + x_{\text{PT}}(t) + n(t)\Big]dt. \quad (32)$$

After simplifying the above integral, we express the probability of error for the Q-branch as (see Appendix B)

$$P_{e_Q} = \frac{1}{2}\text{erfc}\Big[\sqrt{\text{SNR}}(A_Q + B_Q)\Big], \quad (33)$$

where

$$A_Q = \frac{\sin(2\pi f_o T_s) - \cos(2\pi f_o T_s) + 1}{2\pi f_o T_s}, \text{ and}$$

$$B_Q = \sum_{i=1}^{N} \frac{\cos[2\pi(f_i - f_o)T_s + \theta_i] - \cos\theta_i}{\sqrt{\text{SIR}_i}\ 2\pi(f_i - f_o)T_s}.$$

Similar to eq. (28), we express the average error probability over a Rayleigh fading for the I-branch as

$$P_{avg_I} = \frac{1}{2}\left[1 - \sqrt{\frac{\Gamma_I}{\Gamma_I+1}}\right], \quad (34)$$

where $\Gamma_I = \text{SNR}(A_I + B_I)^2$.

For the Q-branch, we have

$$P_{avg_Q} = \frac{1}{2}\left[1 - \sqrt{\frac{\Gamma_Q}{\Gamma_Q+1}}\right], \quad (35)$$

where $\Gamma_Q = \text{SNR}(A_Q + B_Q)^2$.

Thus, the overall average probability of error over a Rayleigh fading channel is given by

$$P_{avg} = \frac{1}{4}\left[2 - \sqrt{\frac{\Gamma_I}{\Gamma_I+1}} - \sqrt{\frac{\Gamma_Q}{\Gamma_Q+1}}\right]. \quad (36)$$

Similarly, we approximately obtain the overall asymptotic average error probability at high SNRs as $P_{avg} \approx \frac{1}{8}[\frac{1}{\Gamma_I} + \frac{1}{\Gamma_Q}]$.

*Special Case II:* When $f_o = 0$, the overall average error probability is given by replacing $\Gamma_I$ and $\Gamma_Q$ with $\Gamma_{I_0}$ and $\Gamma_{Q_0}$, respectively, in eq. (36), where $\Gamma_{I_0} = \text{SNR}(1 + \sum_{i=1}^{N} \frac{\sin[2\pi f_i T_s + \theta_i] - \sin\theta_i}{\sqrt{\text{SIR}_i}\ 2\pi f_i T_s})^2$ and $\Gamma_{Q_0} = \text{SNR}(1 + \sum_{i=1}^{N} \frac{\cos[2\pi f_i T_s + \theta_i] - \cos\theta_i}{\sqrt{\text{SIR}_i}\ 2\pi f_i T_s})^2$.

### C. MSK

The MSK demodulation is also implemented via an I/Q architecture, similar to QPSK. By using the same approach as previously, the integrator output for the I-branch assuming an AWGN channel is expressed as

$$r_I = \int_{-T_b}^{T_b} \sqrt{\frac{2}{T_b}}\cos\left(\frac{\pi t}{2T_b}\right)\cos(w_c t + w_o t) \times \Big[x_{\text{IT}_m}(t) + x_{\text{PT}}(t) + n(t)\Big]dt. \quad (37)$$

After simplifying the above integral (see Appendix C), we get

$$r_I = \sqrt{E_b}(C_I + D_I) + N_0, \quad (38)$$

where

$$C_I = \frac{\sin(2\pi f_o T_b)(1 - f_o T_b)}{2\pi f_o T_b\big(1 - (2f_o T_b)^2\big)}, \text{ and}$$

$$D_I = \sum_{i=1}^{N} \frac{4\cos\theta_i \cos(2\pi(f_i - f_o)T_b)}{\pi\sqrt{\text{SIR}_i}\left[1 - (4(f_i - f_o)T_b)^2\right]}.$$

The probability of error for the I-branch is obtained as

$$P_{e_I} = \frac{1}{2}\text{erfc}\left[\sqrt{\text{SNR}}(C_I + D_I)\right]. \tag{39}$$

Now for the Q-branch, the integrator output is given as

$$r_Q = \int_0^{2T_b} \sqrt{\frac{2}{T_b}} \sin\left(\frac{\pi t}{2T_b}\right) \sin(w_c t + w_o t) \times \left[x_{\text{IT}_m}(t) + x_{\text{PT}}(t) + n(t)\right]dt. \tag{40}$$

After simplification, the probability of error for Q-branch is obtained as (see Appendix C)

$$P_{e_Q} = \frac{1}{2}\text{erfc}\left[\sqrt{\text{SNR}}(C_Q - D_Q)\right], \tag{41}$$

where

$$C_Q = \frac{\sin(4\pi f_o T_b) + 2f_o T_b \sin(2\pi f_o T_b)}{4\pi f_o T_b\left(1 - (2f_o T_b)^2\right)}, \text{ and}$$

$$D_Q = \sum_{i=1}^{N} \frac{2\left[\sin(4\pi(f_i - f_o)T_b + \theta_i) + \sin\theta_i\right]}{\pi\sqrt{\text{SIR}_i}\left[1 - (4(f_i - f_o)T_b)^2\right]}.$$

Similar to eq. (36), the overall average error probability over a Rayleigh fading channel is obtained as

$$P_{avg} = \frac{1}{4}\left[2 - \sqrt{\frac{\bar{\Gamma}_I}{\bar{\Gamma}_I + 1}} - \sqrt{\frac{\bar{\Gamma}_Q}{\bar{\Gamma}_Q + 1}}\right], \tag{42}$$

where $\bar{\Gamma}_I = \text{SNR}(C_I + D_I)^2$ and $\bar{\Gamma}_Q = \text{SNR}(C_Q - D_Q)^2$. Now, at high SNRs, the overall asymptotic average error probability is given as $P_{avg} \approx \frac{1}{8}[\frac{1}{\bar{\Gamma}_I} + \frac{1}{\bar{\Gamma}_Q}]$.

*Special Case III:* When $f_o = 0$, the overall average error probability is given by replacing $\bar{\Gamma}_I$ and $\bar{\Gamma}_Q$ with $\bar{\Gamma}_{I_0}$ and $\bar{\Gamma}_{Q_0}$, respectively, in eq. (42), where $\bar{\Gamma}_{I_0} = \text{SNR}(1 + \sum_{i=1}^{N} \frac{4\cos\theta_i\cos(2\pi f_i T_b)}{\pi\sqrt{\text{SIR}_i}[1-(4f_i T_b)^2]})^2$ and $\bar{\Gamma}_{Q_0} = \text{SNR}(1 + \sum_{i=1}^{N} \frac{2[\sin(4\pi f_i T_b+\theta_i)+\sin\theta_i]}{\pi\sqrt{\text{SIR}_i}[1-(4f_i T_b)^2]})^2$.

### D. 16-QAM

The 16-QAM demodulator is another example of an I/Q demodulation architecture. By assuming initially an AWGN channel as previously, the integrator output for the I-branch is expressed as

$$r_I = \int_0^{T_s} \sqrt{\frac{2}{T_s}} \cos(w_c t + w_o t) \times \left[x_{\text{IT}_{\tilde{q}}}(t) + x_{\text{PT}}(t) + n(t)\right]dt. \tag{43}$$

After simplifying the above integral (see Appendix D), we obtain the probability of error for the I-branch as

$$P_{e_I} \approx \frac{3}{8}\text{erfc}\left[\sqrt{\text{SNR}}\left(\sqrt{\frac{2}{5}}A_I + \frac{B_I}{\sqrt{5}}\right)\right]. \tag{44}$$

Now, the integrator output for the Q-branch is given as

$$r_Q = \int_0^{T_s} \sqrt{\frac{2}{T_s}} \sin(w_c t + w_o t) \times \left[x_{\text{IT}_{\tilde{q}}}(t) + x_{\text{PT}}(t) + n(t)\right]dt. \tag{45}$$

The probability of error for the Q-branch is obtained as (see Appendix D)

$$P_{e_Q} \approx \frac{3}{8}\text{erfc}\left[\sqrt{\text{SNR}}\left(\sqrt{\frac{2}{5}}A_Q + \frac{B_Q}{\sqrt{5}}\right)\right]. \tag{46}$$

Similar to eq. (36), the overall average error probability over a Rayleigh fading channel is obtained as

$$P_{avg} = \frac{3}{16}\left[2 - \sqrt{\frac{\tilde{\Gamma}_I}{\tilde{\Gamma}_I + 1}} - \sqrt{\frac{\tilde{\Gamma}_Q}{\tilde{\Gamma}_Q + 1}}\right], \tag{47}$$

where $\tilde{\Gamma}_I = \text{SNR}(\sqrt{\frac{2}{5}}A_I + \frac{B_I}{\sqrt{5}})^2$ and $\tilde{\Gamma}_Q = \text{SNR}(\sqrt{\frac{2}{5}}A_Q + \frac{B_Q}{\sqrt{5}})^2$. In the same way, we obtain the overall asymptotic average error probability at high SNRs as $P_{avg} \approx \frac{3}{32}[\frac{1}{\tilde{\Gamma}_I} + \frac{1}{\tilde{\Gamma}_Q}]$.

*Special Case IV:* When $f_o = 0$, the overall average error probability is given by replacing $\tilde{\Gamma}_I$ and $\tilde{\Gamma}_Q$ with $\tilde{\Gamma}_{I_0}$ and $\tilde{\Gamma}_{Q_0}$, respectively, in eq. (47), where $\tilde{\Gamma}_{I_0} = \text{SNR}(\sqrt{\frac{2}{5}} + \sum_{i=1}^{N} \frac{\sin[2\pi f_i T_s+\theta_i]-\sin\theta_i}{\sqrt{5}\sqrt{\text{SIR}_i}\ 2\pi f_i T_s})^2$ and $\tilde{\Gamma}_{Q_0} = \text{SNR}(\sqrt{\frac{2}{5}} + \sum_{i=1}^{N} \frac{\cos[2\pi f_i T_s+\theta_i]-\cos\theta_i}{\sqrt{5}\sqrt{\text{SIR}_i}\ 2\pi f_i T_s})^2$.

### E. IMPACT OF FREQUENCY OFFSET AND MULTITONE INTERFERENCE

The above analysis investigates the deterioration of the overall performance of the proposed FD-SWIPT system due to the presence of carrier frequency offset and multitone interference. Equations (28), (36), (42), and (47) have shown that the presence of a frequency offset leads to a decrease in SNR. Moreover, as the synchronization error increases, the tones' frequencies also start to deviate from their optimal values, resulting in higher multitone interference and, therefore, higher error probability. In the ideal case where $f_o = 0$, only the multitone interference term is present. In order to minimize the multitone interference, the tones of the energy signal should be placed at the spectral null frequencies or within the low-power sub-band of the data signal, as shown in Fig. 1. Thus, by placing the energy tones at the appropriate locations, we can harvest more power by lowering the value of SIR, as dictated by the spectral power regulations. Table 2 presents a summary of the error rate analysis for the proposed FD-SWIPT waveforms.

## IV. MODULATION CLASSIFICATION AND OPTIMIZATION OF MULTITONE SIGNALS

### A. MODULATION CLASSIFICATION

In this subsection, we present the adopted MC method for the data signals that are superimposed with a multitone energy signal in the proposed FD-SWIPT waveform. The MC is

**TABLE 2.** Summary of error rate analysis.

| Frequency offset ($f_o$) | OVERALL AVERAGE ERROR PROBABILITY | No frequency offset ($f_o = 0$) |
|---|---|---|
| | **BPSK-SWIPT** | |
| $P_{avg} = \frac{1}{2}\left[1 - \sqrt{\frac{\Gamma}{\Gamma+1}}\right]$ | | By replacing $\Gamma$ with $\Gamma_0$ |
| $\Gamma = \text{SNR}\left(\frac{\sin(2\pi f_o T_b)}{2\pi f_o T_b} + \sum_{i=1}^{N} \frac{\sin[2\pi(f_i - f_o)T_b + \theta_i] - \sin\theta_i}{\sqrt{\text{SIR}_i}\ 2\pi(f_i - f_o)T_b}\right)^2$ | | $\Gamma_0 = \text{SNR}\left(1 + \sum_{i=1}^{N} \frac{\sin[2\pi f_i T_b + \theta_i] - \sin\theta_i}{\sqrt{\text{SIR}_i}\ 2\pi f_i T_b}\right)^2$ |
| | **QPSK-SWIPT** | |
| $P_{avg} = \frac{1}{4}\left[2 - \sqrt{\frac{\Gamma_I}{\Gamma_I+1}} - \sqrt{\frac{\Gamma_Q}{\Gamma_Q+1}}\right]$ | | By replacing $\Gamma_I$ and $\Gamma_Q$ with $\Gamma_{I_0}$ and $\Gamma_{Q_0}$, respectively |
| $\Gamma_I = \text{SNR}\left(\frac{\sin(2\pi f_o T_s) + \cos(2\pi f_o T_s) - 1}{2\pi f_o T_s} + \sum_{i=1}^{N} \frac{\sin[2\pi(f_i - f_o)T_s + \theta_i] - \sin\theta_i}{\sqrt{\text{SIR}_i}\ 2\pi(f_i - f_o)T_s}\right)^2$ | | $\Gamma_{I_0} = \text{SNR}\left(1 + \sum_{i=1}^{N} \frac{\sin[2\pi f_i T_s + \theta_i] - \sin\theta_i}{\sqrt{\text{SIR}_i}\ 2\pi f_i T_s}\right)^2$ |
| $\Gamma_Q = \text{SNR}\left(\frac{\sin(2\pi f_o T_s) - \cos(2\pi f_o T_s) + 1}{2\pi f_o T_s} + \sum_{i=1}^{N} \frac{\cos[2\pi(f_i - f_o)T_s + \theta_i] - \cos\theta_i}{\sqrt{\text{SIR}_i}\ 2\pi(f_i - f_o)T_s}\right)^2$ | | $\Gamma_{Q_0} = \text{SNR}\left(1 + \sum_{i=1}^{N} \frac{\cos[2\pi f_i T_s + \theta_i] - \cos\theta_i}{\sqrt{\text{SIR}_i}\ 2\pi f_i T_s}\right)^2$ |
| | **MSK-SWIPT** | |
| $P_{avg} = \frac{1}{4}\left[2 - \sqrt{\frac{\bar{\Gamma}_I}{\bar{\Gamma}_I+1}} - \sqrt{\frac{\bar{\Gamma}_Q}{\bar{\Gamma}_Q+1}}\right]$ | | By replacing $\bar{\Gamma}_I$ and $\bar{\Gamma}_Q$ with $\bar{\Gamma}_{I_0}$ and $\bar{\Gamma}_{Q_0}$, respectively |
| $\bar{\Gamma}_I = \text{SNR}\left(\frac{\sin(2\pi f_o T_b)(1 - f_o T_b)}{2\pi f_o T_b(1-(2f_o T_b)^2)} + \sum_{i=1}^{N} \frac{4\cos\theta_i \cos(2\pi(f_i - f_o)T_b)}{\pi\sqrt{\text{SIR}_i}[1-(4(f_i - f_o)T_b)^2]}\right)^2$ | | $\bar{\Gamma}_{I_0} = \text{SNR}\left(1 + \sum_{i=1}^{N} \frac{4\cos\theta_i \cos(2\pi f_i T_b)}{\pi\sqrt{\text{SIR}_i}[1-(4f_i T_b)^2]}\right)^2$ |
| $\bar{\Gamma}_Q = \text{SNR}\left(\frac{\sin(4\pi f_o T_b) + 2 f_o T_b \sin(2\pi f_o T_b)}{4\pi f_o T_b(1-(2f_o T_b)^2)} - \sum_{i=1}^{N} \frac{2[\sin(4\pi(f_i - f_o)T_b + \theta_i) + \sin\theta_i]}{\pi\sqrt{\text{SIR}_i}[1-(4(f_i - f_o)T_b)^2]}\right)^2$ | | $\bar{\Gamma}_{Q_0} = \text{SNR}\left(1 + \sum_{i=1}^{N} \frac{2[\sin(4\pi f_i T_b + \theta_i) + \sin\theta_i]}{\pi\sqrt{\text{SIR}_i}[1-(4f_i T_b)^2]}\right)^2$ |
| | **16-QAM-SWIPT** | |
| $P_{avg} = \frac{3}{16}\left[2 - \sqrt{\frac{\tilde{\Gamma}_I}{\tilde{\Gamma}_I+1}} - \sqrt{\frac{\tilde{\Gamma}_Q}{\tilde{\Gamma}_Q+1}}\right]$ | | By replacing $\tilde{\Gamma}_I$ and $\tilde{\Gamma}_Q$ with $\tilde{\Gamma}_{I_0}$ and $\tilde{\Gamma}_{Q_0}$, respectively |
| $\tilde{\Gamma}_I = \text{SNR}\left(\sqrt{\frac{2}{5}}\frac{\sin(2\pi f_o T_s) + \cos(2\pi f_o T_s) - 1}{2\pi f_o T_s} + \sum_{i=1}^{N} \frac{\sin[2\pi(f_i - f_o)T_s + \theta_i] - \sin\theta_i}{\sqrt{5}\sqrt{\text{SIR}_i}\ 2\pi(f_i - f_o)T_s}\right)^2$ | | $\tilde{\Gamma}_{I_0} = \text{SNR}\left(\sqrt{\frac{2}{5}} + \sum_{i=1}^{N} \frac{\sin[2\pi f_i T_s + \theta_i] - \sin\theta_i}{\sqrt{5}\sqrt{\text{SIR}_i}\ 2\pi f_i T_s}\right)^2$ |
| $\tilde{\Gamma}_Q = \text{SNR}\left(\sqrt{\frac{2}{5}}\frac{\sin(2\pi f_o T_s) - \cos(2\pi f_o T_s) + 1}{2\pi f_o T_s} + \sum_{i=1}^{N} \frac{\cos[2\pi(f_i - f_o)T_s + \theta_i] - \cos\theta_i}{\sqrt{5}\sqrt{\text{SIR}_i}\ 2\pi(f_i - f_o)T_s}\right)^2$ | | $\tilde{\Gamma}_{Q_0} = \text{SNR}\left(\sqrt{\frac{2}{5}} + \sum_{i=1}^{N} \frac{\cos[2\pi f_i T_s + \theta_i] - \cos\theta_i}{\sqrt{5}\sqrt{\text{SIR}_i}\ 2\pi f_i T_s}\right)^2$ |

based on the DFT of the absolute value of $y[n]$, where $y[n]$ refers to the discrete baseband equivalent of $y(t)$ obtained via uniform sampling at times $t = nT_s$ with $T_s$ denoting the sampling interval. The DFT operation, which can be efficiently implemented by using the fast Fourier transform (FFT) algorithm, plays the role of a feature extraction tool in this application: it exploits the location of the embedded multitone energy signal to classify the proposed FD-SWIPT waveforms. It can be expressed as

$$\hat{R}[f] = \frac{1}{K}\sum_{n=0}^{K-1} |y[n]| e^{-j2\pi nf}, \tag{48}$$

where $K$ is the DFT size. Once $\hat{R}[f]$ is computed, the non-zero peak frequency is estimated as $\hat{f} = \arg\ \max|\hat{R}[f]_{f\in[u,v]}|$, where $u = f_{bw}KT_s/2$ and $v = 4f_{bw}KT_s$ are the lower and upper interval boundaries, respectively, and $f_{bw}$ denotes the 3 dB signal bandwidth, obtained simply from the PSD of the received signal [15]. Fig. 3 shows the distinctive features of the proposed FD-SWIPT waveforms with a two-tones energy signal for different modulation formats. It is observed that a non-zero peak frequency for BPSK-, QPSK-, 16-QAM-, and MSK-FD-SWIPT appears at $\hat{f} = 1.9f_s$, $\hat{f} = 1.8f_s$, $\hat{f} = 1.6f_s$, and $\hat{f} = 1.4f_s$, respectively. Thus, we can efficiently classify the proposed FD-SWIPT waveforms via the FFT algorithm.

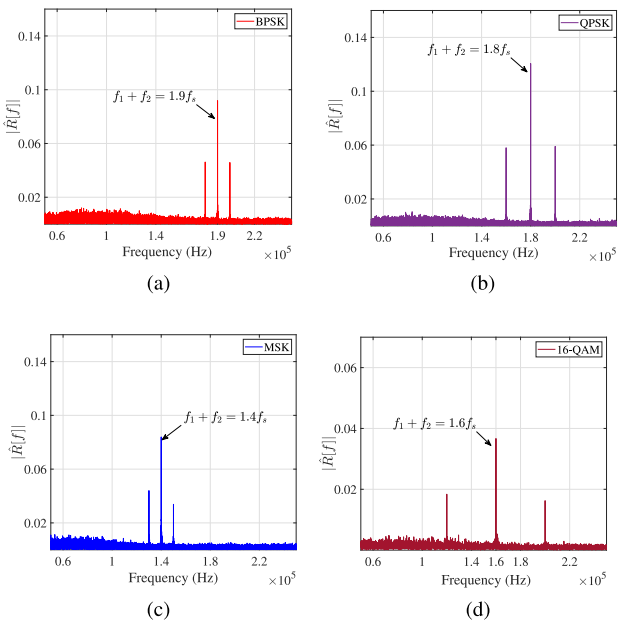


**FIGURE 3.** Non-zero peak frequency of the proposed FD-SWIPT waveforms with a two-tones energy signal for different modulation formats: (a) BPSK; (b) QPSK; (c) MSK; (d) 16-QAM.

### B. DESIGN AND OPTIMIZATION OF THE PT SIGNAL

We consider an FD-SWIPT waveform with $N$ energy tones and a normalized tone spacing equal to $\Delta = f_i T_b - f_{i+1} T_b$. A low-power sub-band of the IT signal is defined as the frequency interval $[f_x, f_y]$ within which $S(f) \leq \lambda$, where $f_x < f_y$ and $f_y$ corresponds to the location of a spectral null. Thus, in order to place the PT signal's tones, we use the following approach: we place the first tone at $f_y$ and then we move towards $f_x$ placing tones with step $\Delta$ until all tones are placed within this sub-band or a tone is placed outside this interval. In the latter case, we place this tone (and any other remaining tones) at another low-power sub-band using the same procedure, until all tones are placed.

Next, we focus on the optimization of the tones' power, such that the instantaneous SIR of the IT signal is maximized (and, therefore, *the degrading effect of the multitone interference to the error rate performance is minimized*) subject to the EH and tones' power constraints. Note that $P = P_{\text{IT}} + P_{\text{PT}} \Leftrightarrow P_{\text{PT}} = P - P_{\text{IT}} \Leftrightarrow \sum_{i=1}^{N} P_i = P - S^2 = P_{\text{T}}$, where $P_{\text{IT}} = S^2$ denotes the power of the IT signal, $P_{\text{PT}} = \sum_{i=1}^{N} P_i$ represents the power of the PT signal, $P_i = \alpha_i^2$ is the power of the $i$-th tone, and $P_{\text{T}} = P - S^2$ corresponds to the effective power budget of the PT signal, $i = 1, \ldots, N$. The SIR of the IT signal is given by $\text{SIR} = P_{\text{IT}}/P_{\text{PT}} = S^2/\sum_{i=1}^{N} P_i$. Since $S^2$ is fixed, instead of maximizing the SIR, we can equivalently minimize $P_{\text{PT}}$. To this end, we let $P_{\text{PT}} \leq P_{\text{T}}$. This essentially means that we let the transmit power $P$ to get reduced, if required, without affecting though the power of the IT signal. At the same time, we want to ensure that $P_{\text{DC}} \geq E$, where $E > 0$ is the minimum required harvested power, and $P_i \leq \lambda \ \forall i$.

Based on the above and assuming a local oscillators-based EH circuit, the optimization problem is formulated as:

$$\text{(P1):} \min_{\{P_i \geq 0\}} \ sum_{i=1}^{N} P_i \tag{49a}$$

$$\text{s.t.} \ |h|^2 \sum_{i=1}^{N} P_i \geq E, \tag{49b}$$

$$\sum_{i=1}^{N} P_i \leq P_T, \tag{49c}$$

$$P_i \leq \lambda, \ i = 1, \ldots, N. \tag{49d}$$

Let's consider now a PS-SWIPT receiver where the RF-to-DC energy conversion unit is implemented as a diodes-based rectifier. Under a linear piecewise EH model, we have to replace the left-hand side of Eq. (49b) by Eq. (20), with $P_r$ given by Eq. (18) by replacing $P$ with $\sum_{i=1}^{N} P_i + S^2$. Under a parametric EH model, on the other hand, we have to replace Eq. (49b) by $|h|^2(\sum_{i=1}^{N} P_i + S^2) \geq P_{\text{DC}}^{-1}(E) \triangleq \bar{E}$, where $P_{\text{DC}}$ is given by Eq. (21) and $\bar{E} > 0$. The solution of these optimization problems results to an equal power allocation among the $N$ tones.

## V. EXPERIMENTS AND SIMULATIONS

### A. TESTBED SETUP AND EXPERIMENTAL VALIDATION

As mentioned earlier, the proposed FD-SWIPT technique is suitable for application in systems with conventional COTS receivers that make use of a diodes-based rectifier. In this section, we experimentally validate this argument in an indoor propagation environment. The SDR-based prototype testbed setup is shown in Fig. 4. The testbed implementation chain is divided into hardware and software modules. The hardware consists of a personal computer that displays the results of the experiment; a National Instruments (NI) universal software radio peripheral (USRP)-2920, which acts as the transmitter as well as the ID branch of the receiver; a powercast P21XXCSR-EVB evaluation board, which plays the role of the EH circuit, harvesting the RF power of the received composite signal and converting it to DC power via a diodes-based rectifier followed by a LPF; and a microchip MRF24J40 access point, which sends these values to the personal computer [36], [37]. The software refers to the RealTerm and LabVIEW programs. The former is required to display the harvested DC power values, while the latter provides transmitter-receiver configuration capabilities and allows us to feed the experimental data to LabVIEW-embedded MATLAB scripts for performance evaluation purposes [38]. The system has one antenna at the transmitter for information transfer and two antennas at the receiver, one connected to the EH branch and another connected to the ID branch. Note that *the software emulates the two separate ID and EH receivers as a single device with collocated ID and EH units*, although under the purpose of this experiment it doesn't really matter whether we consider a separate receivers architecture or a PS-SWIPT one with collocated ID/EH units. Furthermore, the former setup is just a special case of PS-SWIPT with $\rho = 1$ and, therefore, $1 - \rho = 0$. The experimental setup is described in Table 3.

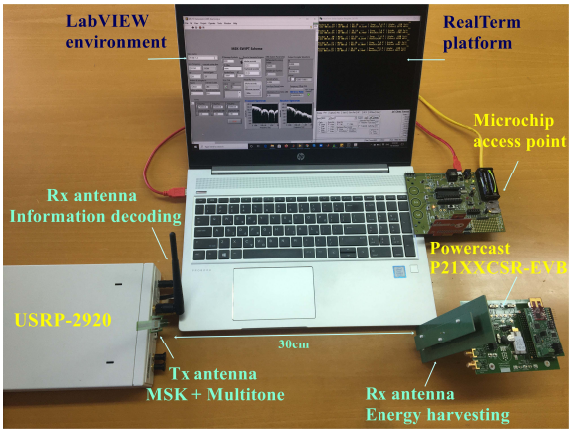


**FIGURE 4.** SDR-based prototype testbed setup.

**TABLE 3.** Experimental setup.

| Hardware Configuration | Details |
|---|---|
| Computer | Hp Probook 16GB RAM |
| | Core i5 processor |
| SDR | USRP-2920 |
| RF energy harvester | Powercast P21XXCSR |
| Access point | Microchip MRF24J40 |
| **Experimental parameters** | |
| RF carrier frequency | 915 MHz |
| Sampling rate | 1 MSamples/s |

The transmitter consists of a USRP-2920 unit and the LabVIEW software. It broadcasts an FD-SWIPT RF signal with a center frequency $f_c = 915$ MHz, which corresponds to the carrier frequency of the modulation signal and it is a standardized frequency of operation for powercast devices [37].

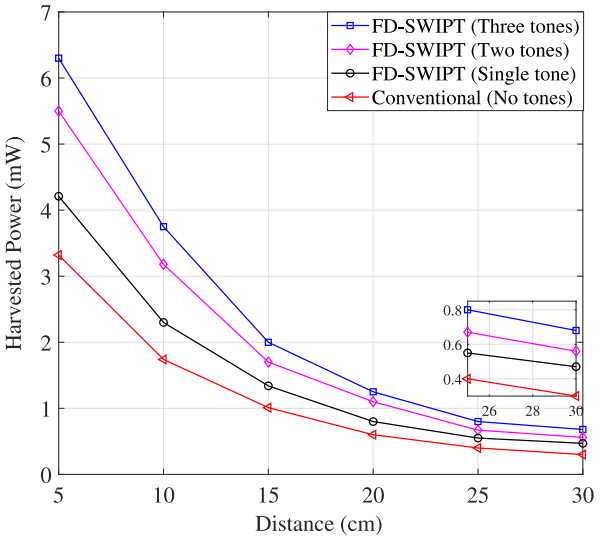


**FIGURE 5.** Harvested power vs. Tx-Rx distance for different number of energy tones assuming a 30 dB transmission gain.

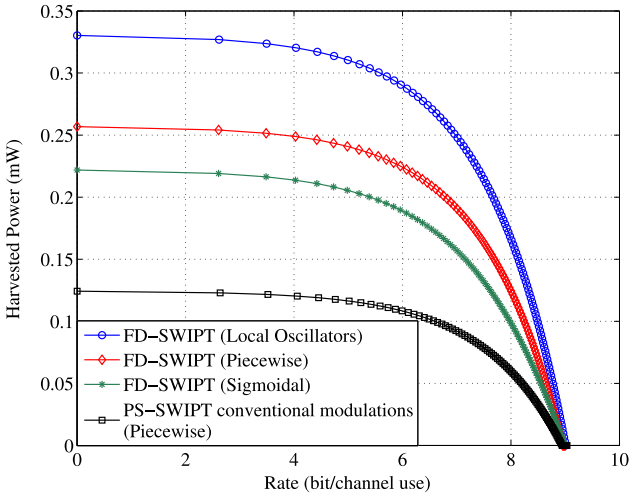


**FIGURE 6.** Rate-Energy region of the proposed FD-SWIPT for different receivers and EH models.

The transmit gain, RF carrier frequency, sampling rate, and modulation can be easily changed in LabVIEW.

The receiver consists of a USRP-2920 unit, a P21XXCSR-EVB board, a microchip MRF24J40 access point, LabVIEW, and RealTerm. We initially turn our attention to the ID branch. RF signal acquisition-related parameters are configured via LabVIEW. These include the start trigger time, the carrier frequency, the receive gain, and the sampling rate. The received RF signal is then down-converted to the baseband. The processing of the baseband signal is controlled by the LabVIEW MathScript in realtime. Next, the digitized received signal is fed to a LabVIEW-embedded MATLAB script, which enables us to run various numerical simulations and assess, for instance, the average error probability or the information rate. Then, the MC algorithm is performed to classify the proposed FD-SWIPT modulations. Finally, NI-USRP modulation toolkit modules are used in the ID branch to retrieve the original transmitted signal (i.e., to perform demodulation).

In the EH branch, the relevant receiver components are the powercast P21XXCSR-EVB sensor board and the microchip access point for wireless power transfer, as mentioned previously. Powercast first converts the RF energy to regulated DC. This DC information is read by the sensor board and is converted into a data packet. Then, this packet is sent by an on-board microchip RF transceiver to the microchip access point by using the MiWi point-to-point low power protocol [37]. Finally, the collected sensor data are sent by the microchip access point to the personal computer via a universal serial bus connection and are displayed using the RealTerm software.

In the experiment, we varied the distance between the transmitter and the receiver and fixed the USRP transmission gain at 30 dB. Each transmission frame lasted approximately 300 seconds and we displayed the average harvested power at each instant. Fig. 5 shows the harvested power as a function of transmitter-receiver (Tx-Rx) distance for different waveforms with varying number of multitones. *This test demonstrates the validity of the proposed technique, even under a diodes-based EH circuit implementation*. It is also observed that by superimposing more energy tones, for a given transmit power, we can harvest more power, as expected, due to the high peak to average power ratio (PAPR) of the multitone energy signal which improves the overall energy conversion efficiency of the proposed FD-SWIPT system under the non-linearities of the diodes-based rectifier. It is also noted that the performance degrades as the propagation distance increases, as expected.

### B. NUMERICAL SIMULATIONS

We evaluate the performance of the proposed FD-SWIPT system through numerical simulations. We assume a Rayleigh block fading channel with a unit variance. We set the sampling rate at 1 MSamples/s and consider 10 samples per symbol. The phases $\theta_i$ follow a uniform distribution in $[0, 2\pi]$, while the normalized tone spacing is $\Delta = 0.1$. The RF-EH conversion efficiency, sensitivity and saturation thresholds, and receive noise variance are set to 0.8, $-20$ dBm, 10 dBm, and $-35$ dBm, respectively [33], [34]. The EH circuit specifications are $a_1 = 1500$ and $a_2 = 0.0022$ [34]. We consider $10^5$ iterations with 10000 transmitted samples in each one.

In Fig. 6, we plot the rate–energy (R–E) region of an FD-SWIPT waveform consisting of an IT signal and a superimposed three-tones PT signal for the cases where an LOs-based receiver is employed (blue curve) or a conventional PS-SWIPT receiver that utilizes a diodes-based rectifier is adopted, assuming either a piecewise (red curve) or a sigmoidal (purple curve) EH model in the latter scenario. We also plot the R–E region for the piecewise EH model case when a pure IT signal (without PT tones superimposed on it) is transmitted (black curve). Since in the PS-based receiver only a portion of the received RF power is fed to the EH circuit, we scale the power at the EH and ID branches of

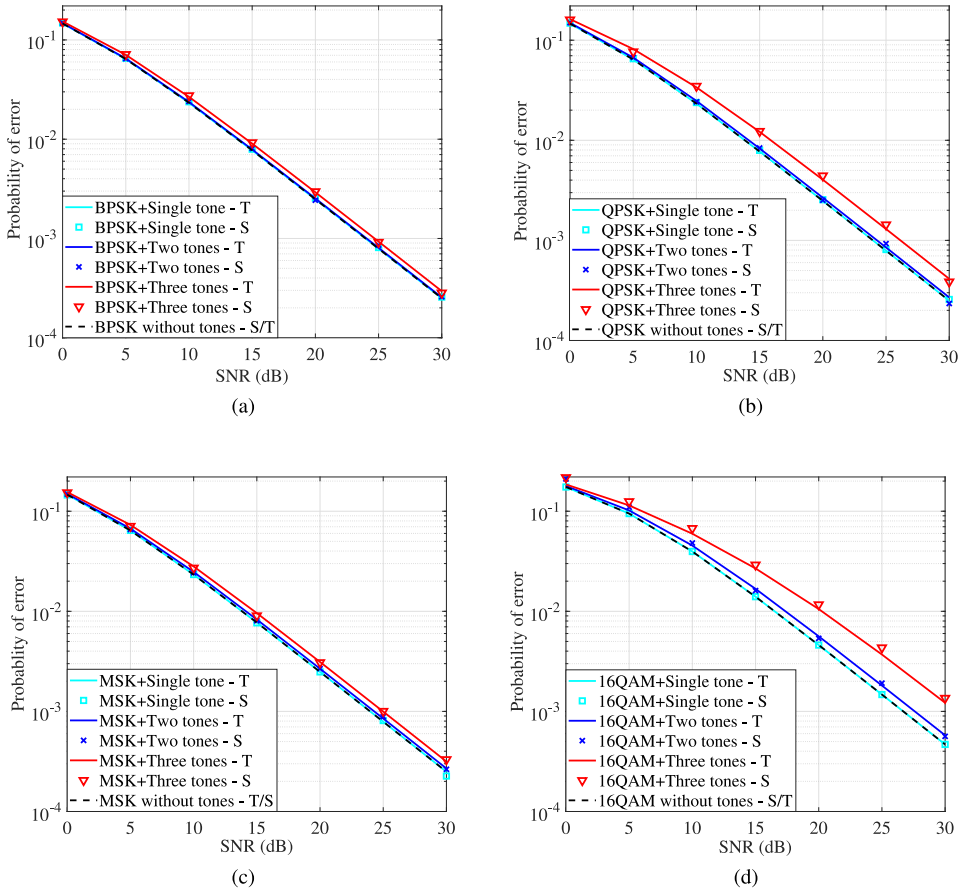


**FIGURE 7.** $P_e$ vs. SNR: Theoretical vs. simulation results for (a) BPSK-FD-SWIPT, (b) QPSK-FD-SWIPT, (c) MSK-FD-SWIPT, and (d) 16-QAM-FD-SWIPT.

the LOs-based receiver accordingly, for comparison fairness purposes (i.e., to remove the inefficiency of PS-SWIPT from our comparisons). We note that: i) the LOs-based receiver (blue curve) harvests more power than the diodes-based rectifier regardless of the considered EH model (red and purple curves), due to the lower energy conversion efficiency of the latter; and ii) the transmission of a multitone PT signal along with the IT signal improves the energy rate when a diodes-based rectifier is used (red and purple curves vs. black curve), as expected, due to the non-linearities of the rectifier.

Fig. 7 plots both the simulated (S) and the theoretical (T) probability of error ($P_e$) for BPSK-, QPSK-, MSK-, 16-QAM-FD-SWIPT versus SNR, respectively. It is observed that the FD-SWIPT waveform achieves the same error rate performance with a corresponding modulation signal, i.e., *with proper design, the multitone interference is negligible*. As we shift the tones of the PT signal to the high-power sub-bands, however, we notice that the error probability starts to increase, as expected, due to the higher interference levels.

Fig. 8 repeats the previous test in the presence of a frequency synchronization error. The frequency offset is normalized to the symbol rate ($\epsilon = f_o/f_s$). It is noticed that for a low value of $\epsilon$, the FD-SWIPT waveform can achieve the same error performance with a corresponding modulation signal. *As the synchronization error increases, the error probability starts to increase as well*, as expected, since the incurred multitone interference gets higher as the tones' frequencies start to deviate from their optimal values.

Fig. 9a presents the probability of error versus the SNR for a Gaussian MSK (GMSK[1])-FD-SWIPT waveform. It is observed that *GMSK-FD-SWIPT can achieve almost the same error performance as the MSK-FD-SWIPT waveform.*

Fig. 9b illustrates the percentage of correct modulation classification ($P_{cc}$) versus SNR for the proposed FD-SWIPT waveform. The modulation classifier requires only 1000 symbols to work with sufficient precision. It is noticed that *the MC performance is good even at low SNR* (especially for QPSK), *thus demonstrating again that the multitone interference is negligible*, and improves exponentially with the SNR until it eventually converges to a floor, as expected.

1. GMSK is obtained by filtering the MSK modulation with a Gaussian filter. This results in a better utilization of the available frequency spectrum. Also, GMSK is resilient against non-linear amplifier distortion. It has been adopted by the GSM [39] and Bluetooth standards.

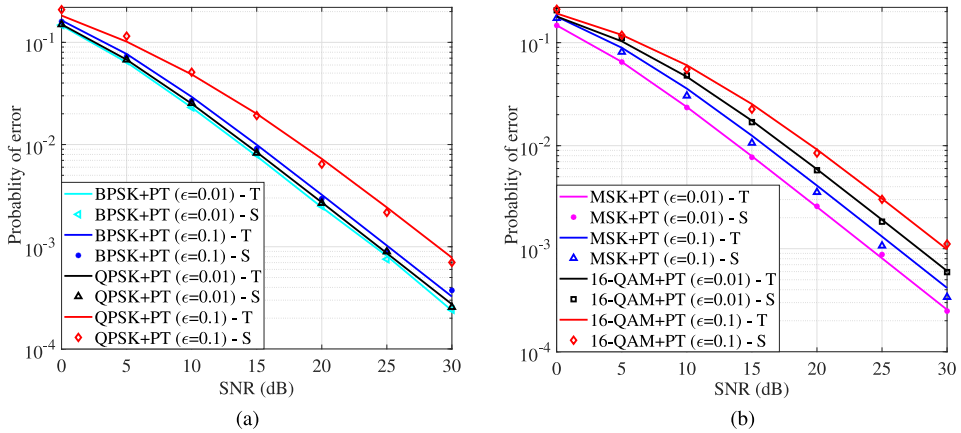


**FIGURE 8.** $P_e$ vs. SNR: Theoretical vs. simulation results in the presence of frequency synchronization error with a two-tones energy signal and (a) a BPSK or QPSK modulation signal; (b) a MSK- or 16-QAM modulation signal.

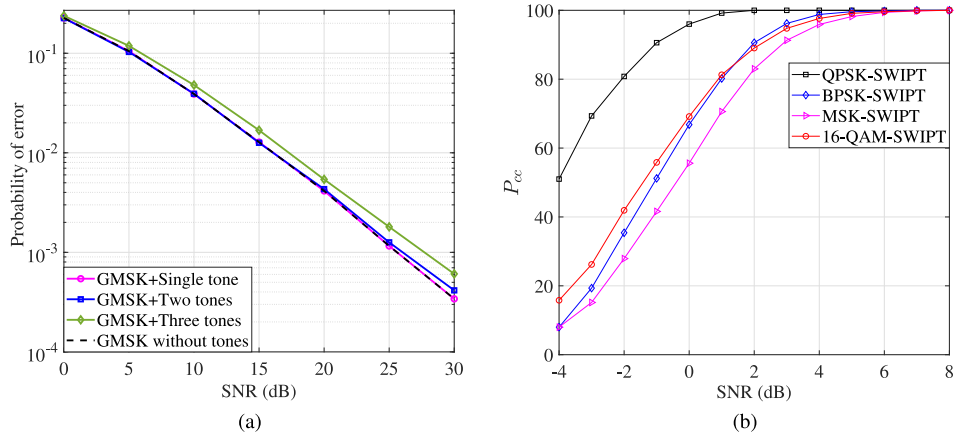


**FIGURE 9.** (a) $P_e$ vs. SNR: Simulation results for GMSK-SWIPT. (b) Percentage of correct modulation classification vs. SNR: Simulation results of the proposed FD-SWIPT waveform with a two-tones energy signal.

## VI. CONCLUSION

In this paper, we presented a novel FD-SWIPT waveform design that supports EH circuit implementations based either on rectifying diodes or local oscillators and allows the application of an FB-MC scheme based on the DFT at the receiver. The average error probability under various modulation schemes was derived in the presence of frequency synchronization errors, multitone interference, and Rayleigh fading. Numerical simulations have shown that by placing the tones of the energy signal at the spectral nulls and/or low-power sub-bands of the modulation signal, we can significantly increase the harvested power and the data rate in comparison to the conventional PS-SWIPT approach without using notch/peak receive filters as well as closely approximate the error rate performance of pure modulation signals and achieve MC with sufficiently high precision, thanks to the minimization of the multitone interference. The proposed design was experimentally validated via real-world measurements in an indoor propagation environment. In the future, we plan to extend this work by studying the performance of an FD-SWIPT waveform that utilizes a multi-carrier IT signal.

## APPENDIX A
## PROOF OF EQS. (26) AND (28)

By Substituting $x_{\mathrm{IT}_b}(t)$ and $x_{\mathrm{PT}}(t)$ in Eq. (24), we obtain

$$\begin{aligned} r &= \int_0^{T_b} \sqrt{\frac{2}{T_b}} \cos(w_c t + w_o t) \\ &\quad \times \left\{ \sqrt{\frac{2E_b}{T_b}} \cos(w_c t) + \sum_{i=1}^{N} \alpha_i \cos(w_c t + w_i t + \theta_i) + n(t) \right\} dt \\ &= \frac{\sqrt{E_b}}{T_b} \int_0^{T_b} \cos(w_o t) dt + \sum_{i=1}^{N} \frac{\alpha_i}{\sqrt{2T_b}} \\ &\quad \times \int_0^{T_b} [\cos(w_i t + \theta_i) \times \cos(w_o t) \\ &\qquad + \sin(w_i t + \theta_i) \sin(w_o t)] dt + N_0. \end{aligned} \tag{50}$$

After simplifying the above integral, we have

$$\begin{aligned} r &= \sqrt{E_b} \frac{\sin(w_o T_b)}{w_o T_b} \\ &\quad + \sum_{i=1}^{N} \frac{\alpha_i \sin[(w_i - w_o)T_b + \theta_i] - \sin\theta_i}{\sqrt{2T_b}\ (w_i - w_o)} + N_0, \\ &= \sqrt{E_b}(A + B) + N_0, \end{aligned} \tag{51}$$

where $A$ and $B$ are given in Section III-A. The error probability over an AWGN channel in the presence of frequency offset and multitone interference is obtained as

$$P_e = \frac{1}{2}\text{erfc}\Big[\sqrt{\text{SNR}}(A+B)\Big]. \tag{52}$$

Now from eq. (27), we can find the average error probability over a Rayleigh fading channel as

$$\begin{aligned} P_{avg} &= \int_0^\infty \frac{1}{2}\text{erfc}\Big[\sqrt{b}\sqrt{\text{SNR}}(A+B)\Big]e^{-b}db \\ &= \frac{1}{2}\int_0^\infty \text{erfc}\Big(\sqrt{b\Gamma}\Big)e^{-b}db \\ &\overset{v=b\Gamma}{=} \frac{1}{2\Gamma}\int_0^\infty \text{erfc}\big(\sqrt{v}\big)e^{-\frac{v}{\Gamma}}dv \\ &= \frac{1}{2} - \frac{1}{2\sqrt{\pi}}\int_0^\infty e^{-v\left(\frac{1+\Gamma}{\Gamma}\right)}v^{-1/2}dv \\ &\overset{u=v\left(\frac{1+\Gamma}{\Gamma}\right)}{=} \frac{1}{2} - \frac{1}{2\sqrt{\pi}}\sqrt{\frac{\Gamma}{1+\Gamma}}\int_0^\infty e^{-u}u^{-1/2}du, \end{aligned} \tag{53}$$

where $\Gamma = \text{SNR}(A+B)^2$. Since $\int_0^\infty e^{-u}u^{-1/2}du = \sqrt{\pi}$, we obtain

$$P_{avg} = \frac{1}{2}\left[1 - \sqrt{\frac{\Gamma}{\Gamma+1}}\right]. \tag{54}$$

## APPENDIX B
## PROOF OF EQ. (36)

Substituting $x_{\text{IT}_q}(t)$ and $x_{\text{PT}}(t)$ in eq. (29), we obtain

$$\begin{aligned} r_I = &\frac{\sqrt{E_s}}{T_s}\int_0^{T_s}[\cos(w_o t) - \sin(w_o t)]dt \\ &+ \sum_{i=1}^{N}\frac{\alpha_i}{\sqrt{2T_s}}\int_0^{T_s}[\cos(w_i t+\theta_i)\cos(w_o t) \\ &\qquad + \sin(w_i t+\theta_i)\sin(w_o t)]dt + N_0. \end{aligned} \tag{55}$$

After simplifying the above integral, we have

$$\begin{aligned} r_I &= \sqrt{E_s}\left[\frac{\sin(w_o T_s)}{w_o T_s} + \frac{\cos(w_o T_s)-1}{w_o T_s}\right] \\ &\quad + \sum_{i=1}^{N}\frac{\alpha_i \sin[(w_i-w_o)T_s+\theta_i] - \sin\theta_i}{\sqrt{2T_s}\,(w_i-w_o)} + N_0, \\ &= \sqrt{E_b}(A_I + B_I) + N_0, \end{aligned} \tag{56}$$

where $A_I$ and $B_I$ are given in Section III-B.

Similarly for the Q-branch, by substituting $x_{\text{IT}_q}(t)$ and $x_{\text{PT}}(t)$ in eq. (32), we have

$$\begin{aligned} r_Q = &\frac{\sqrt{E_s}}{T_s}\int_0^{T_s}[\sin(w_o t) + \cos(w_o t)]dt \\ &+ \sum_{i=1}^{N}\frac{\alpha_i}{\sqrt{2T_s}}\int_0^{T_s}[\cos(w_i t+\theta_i)\sin(w_o t) \\ &\qquad + \sin(w_i t+\theta_i)\cos(w_o t)]dt + N_0. \end{aligned} \tag{57}$$

After simplifying the above integral, we have

$$\begin{aligned} r_Q &= \sqrt{E_s}\left[\frac{\sin(w_o T_s)}{w_o T_s} + \frac{1-\cos(w_o T_s)}{w_o T_s}\right] \\ &\quad + \sum_{i=1}^{N}\frac{\alpha_i \cos[(w_i-w_o)T_s+\theta_i] - \cos\theta_i}{\sqrt{2T_s}\,(w_i-w_o)} + N_0, \\ &= \sqrt{E_b}(A_Q + B_Q) + N_0, \end{aligned} \tag{58}$$

where $A_Q$ and $B_Q$ are given in Section III-B.

Finally, the overall error probability over an AWGN channel is obtained as

$$P_e = \frac{1}{4}\text{erfc}\Big[\sqrt{\text{SNR}}(A_I+B_I)\Big] + \frac{1}{4}\text{erfc}\Big[\sqrt{\text{SNR}}(A_Q+B_Q)\Big]. \tag{59}$$

Similar to eq. (54), we can find the average error probability over a Rayleigh fading channel for the I- and Q-branch as

$$P_{avg_I} = \frac{1}{2}\left[1 - \sqrt{\frac{\Gamma_I}{\Gamma_I+1}}\right], P_{avg_Q} = \frac{1}{2}\left[1 - \sqrt{\frac{\Gamma_Q}{\Gamma_Q+1}}\right], \tag{60}$$

where $\Gamma_I$ and $\Gamma_Q$ are given in Section III-B. The overall average probability of error is obtained as $P_{avg} = \frac{P_{avg_I}+P_{avg_Q}}{2}$.

## APPENDIX C
## PROOF OF EQ. (42)

Substituting $x_{\text{IT}_m}(t)$ and $x_{\text{PT}}(t)$ in eq. (37), we obtain

$$\begin{aligned} r_I = &\frac{\sqrt{E_b}}{2T_b}\int_{-T_b}^{T_b}\left[\cos(w_o t) + \cos\left(\frac{\pi t}{T_b}\right)\cos(w_o t)\right]dt \\ &- \frac{\sqrt{E_b}}{2T_b}\int_0^{T_b}\sin\left(\frac{\pi t}{T_b}\right)\sin(w_o t)dt \\ &+ \sum_{i=1}^{N}\frac{\alpha_i}{\sqrt{2T_b}}\int_{-T_b}^{T_b}\left[\cos(w_i t+\theta_i)\cos(w_o t)\cos\left(\frac{\pi t}{2T_b}\right)\right. \\ &\qquad \left. + \sin(w_i t+\theta_i)\sin(w_o t)\cos\left(\frac{\pi t}{2T_b}\right)\right]dt + N_0. \end{aligned} \tag{61}$$

After simplifying the above integral, we have

$$\begin{aligned} r_I &= \sqrt{E_b}\left[\frac{\sin(w_o T_b)}{w_o T_b} + \frac{\sin(w_o T_b)(2w_o T_b - \pi)}{2\left[\pi^2 - (w_o T_b)^2\right]}\right] \\ &\quad + \sum_{i=1}^{N}\frac{4\alpha_i \pi\sqrt{T_b}\cos\theta_i\cos(w_i-w_o)T_b}{\sqrt{2}\left[\pi^2 - 4(w_i-w_o)^2 T_b^2\right]} + N_0, \\ &= \sqrt{E_b}(C_I + D_I) + N_0, \end{aligned} \tag{62}$$

where $C_I$ and $D_I$ are given in Section III-C.

Similarly for the Q-branch, by substituting $x_{\text{IT}_m}(t)$ and $x_{\text{PT}}(t)$ in eq. (40), we have

$$r_Q = \frac{\sqrt{E_b}}{2T_b}\int_0^{2T_b}\left[\cos(w_o t) - \cos\left(\frac{\pi t}{T_b}\right)\cos(w_o t)\right]dt$$

$$+\frac{\sqrt{E_b}}{2T_b}\int_0^{T_b}\sin\left(\frac{\pi t}{T_b}\right)\sin(w_o t)dt + \sum_{i=1}^{N}\frac{\alpha_i}{\sqrt{2T_b}}\int_0^{2T_b}\left[\cos(w_i t+\theta_i)\sin(w_o t)\sin\left(\frac{\pi t}{2T_b}\right) - \sin(w_i t+\theta_i)\cos(w_o t)\sin\left(\frac{\pi t}{2T_b}\right)\right]dt + N_0. \tag{63}$$

After simplification, the above integral is expressed as

$$r_Q = \sqrt{E_b}\left[\frac{\sin(2w_oT_b)}{2w_oT_b} + \frac{\sin(2w_oT_b)w_oT_b}{2\left[\pi^2-(w_oT_b)^2\right]} + \frac{\pi\sin(w_oT_b)}{2\left[\pi^2-(w_oT_b)^2\right]}\right] - \sum_{i=1}^{N}\frac{\alpha_i\pi\sqrt{2T_b}[\sin(w_i-w_o)2T_b+\theta_i)+\sin\theta_i]}{\left[\pi^2-4(w_i-w_o)^2T_b^2\right]} + N_0, = \sqrt{E_b}(C_Q-D_Q)+N_0, \tag{64}$$

where $C_Q$ and $D_Q$ are given in Section III-C. Finally, the overall error probability over an AWGN channel is obtained as

$$P_e = \frac{1}{4}\text{erfc}\left[\sqrt{\text{SNR}}(C_I+D_I)\right] + \frac{1}{4}\text{erfc}\left[\sqrt{\text{SNR}}(C_Q-D_Q)\right]. \tag{65}$$

Similar to (60), the overall average error probability over a Rayleigh fading channel is given by

$$P_{avg} = \frac{1}{4}\left[2-\sqrt{\frac{\bar{\Gamma}_I}{\bar{\Gamma}_I+1}}-\sqrt{\frac{\bar{\Gamma}_Q}{\bar{\Gamma}_Q+1}}\right], \tag{66}$$

where $\bar{\Gamma}_I$ and $\bar{\Gamma}_Q$ are given in Section III-C.

## APPENDIX D
## PROOF OF EQ. (47)

Substituting $x_{\text{IT}_{\bar{q}}}(t)$ and $x_{\text{PT}}(t)$ in eq. (43), we obtain

$$r_I = \frac{1}{T_s}\int_0^{T_s}\left[s_{\bar{q}_1}\cos(w_o t) - s_{\bar{q}_2}\sin(w_o t)\right]dt + \sum_{i=1}^{N}\frac{\alpha_i}{\sqrt{2T_s}}\int_0^{T_s}[\cos(w_i t+\theta_i)\cos(w_o t) + \sin(w_i t+\theta_i)\sin(w_o t)]dt + N_0. \tag{67}$$

After simplifying the above integral, we have

$$r_I = s_{\bar{q}_1}\frac{\sin(w_oT_s)}{w_oT_s} + s_{\bar{q}_2}\frac{\cos(w_oT_s)-1}{w_oT_s} + \sum_{i=1}^{N}\frac{\alpha_i\sin\left[(w_i-w_o)T_s+\theta_i\right]-\sin\theta_i}{\sqrt{2T_s}\ (w_i-w_o)} + N_0. \tag{68}$$

By using the nearest neighbor decision rule [31], the error rate of 16-QAM constellations for the I-branch is obtained as

$$P_{e_I} \approx \frac{3}{8}\text{erfc}\left[\sqrt{\text{SNR}}\left(\sqrt{\frac{2}{5}}A_I + \frac{B_I}{\sqrt{5}}\right)\right]. \tag{69}$$

Similarly for the Q-branch, by substituting $x_{\text{IT}_q}(t)$ and $x_{\text{PT}}(t)$ in eq. (45), we have

$$r_Q = \frac{1}{T_s}\int_0^{T_s}\left[s_{\bar{q}_1}\sin(w_o t) + s_{\bar{q}_2}\cos(w_o t)\right]dt + \sum_{i=1}^{N}\frac{\alpha_i}{\sqrt{2T_s}}\int_0^{T_s}[\cos(w_i t+\theta_i)\sin(w_o t) + \sin(w_i t+\theta_i)\cos(w_o t)]dt + N_0. \tag{70}$$

After simplifying the above integral, we obtain

$$r_Q = s_{\bar{q}_2}\frac{\sin(w_oT_s)}{w_oT_s} + s_{\bar{q}_1}\frac{1-\cos(w_oT_s)}{w_oT_s} + \sum_{i=1}^{N}\frac{\alpha_i\cos\left[(w_i-w_o)T_s+\theta_i\right]-\cos\theta_i}{\sqrt{2T_s}\ (w_i-w_o)} + N_0. \tag{71}$$

Similar to eq. (69), the error probability for the Q-branch is written as

$$P_{e_Q} \approx \frac{3}{8}\text{erfc}\left[\sqrt{\text{SNR}}\left(\sqrt{\frac{2}{5}}A_Q + \frac{B_Q}{\sqrt{5}}\right)\right]. \tag{72}$$

Similar to eq. (60), the overall average error probability over a Rayleigh fading channel is given by

$$P_{avg} = \frac{3}{16}\left[2-\sqrt{\frac{\tilde{\Gamma}_I}{\tilde{\Gamma}_I+1}}-\sqrt{\frac{\tilde{\Gamma}_Q}{\tilde{\Gamma}_Q+1}}\right], \tag{73}$$

where $\tilde{\Gamma}_I$ and $\tilde{\Gamma}_Q$ are given in Section III-D.

## REFERENCES


[1] "IoT connections forecast: The rise of enterprise," GSMA, London, U.K., Rep., Dec. 2019.
[2] *Ericsson Mobility Report*, Ericsson, Stockholm, Sweden, Jun. 2021.
[3] I. Krikidis, S. Timotheou, S. Nikolaou, G. Zheng, D. W. K. Ng, and R. Schober, "Simultaneous wireless information and power transfer in modern communication systems," *IEEE Commun. Mag.*, vol. 52, no. 11, pp. 104–110, Nov. 2014.
[4] X. Lu, P. Wang, D. Niyato, D. I. Kim, and Z. Han, "Wireless networks with RF energy harvesting: A contemporary survey," *IEEE Commun. Surveys Tuts.*, vol. 17, no. 2, pp. 757–789, 2nd Quart., 2015.
[5] B. Clerckx, R. Zhang, R. Schober, D. W. K. Ng, D. I. Kim, and H. V. Poor, "Fundamentals of wireless information and power transfer: From RF energy harvester models to signal and system designs," *IEEE J. Sel. Areas Commun.*, vol. 37, no. 1, pp. 4–33, Jan. 2019.
[6] C. R. Valenta and G. D. Durgin, "Harvesting wireless power: Survey of energy-harvester conversion efficiency in far-field, wireless power transfer systems," *IEEE Microw. Mag.*, vol. 15, no. 4, pp. 108–120, Jun. 2014.
[7] M. S. Trotter, J. D. Griffin, and G. D. Durgin, "Power-optimized waveforms for improving the range and reliability of RFID systems," in *Proc. IEEE Int. Conf. RFID*, Orlando, FL, USA, Apr. 2009, pp. 80–87.
[8] B. Clerckx and E. Bayguzina, "Waveform design for wireless power transfer," *IEEE Trans. Signal Process.*, vol. 64, no. 23, pp. 6313–6328, Dec. 2016.

[9] B. Clerckx, "Wireless information and power transfer: Nonlinearity, waveform design, and rate-energy tradeoff," *IEEE Trans. Signal Process.*, vol. 66, no. 4, pp. 847–862, Feb. 2018.

[10] J. Kim, B. Clerckx, and P. D. Mitcheson, "Signal and system design for wireless power transfer: Prototype, experiment and validation," *IEEE Trans. Wireless Commun.*, vol. 19, no. 11, pp. 7453–7469, Nov. 2020.

[11] R. Gupta, S. Kumar, and S. Majhi, "Blind modulation classification for asynchronous OFDM systems over unknown signal parameters and channel statistics," *IEEE Trans. Veh. Technol.*, vol. 69, no. 5, pp. 5281–5292, May 2020.

[12] O. A. Dobre, A. Abdi, Y. Bar-Ness, and W. Su, "Survey of automatic modulation classification techniques: Classical approaches and new trends," *IET Commun.*, vol. 1, no. 2, pp. 137–156, Apr. 2007.

[13] O. A. Dobre, M. Oner, S. Rajan, and R. Inkol, "Cyclostationarity-based robust algorithms for QAM signal identification," *IEEE Commun. Lett.*, vol. 16, no. 1, pp. 12–15, Jan. 2012.

[14] S. Majhi, R. Gupta, W. Xiang, and S. Glisic, "Hierarchical hypothesis and feature-based blind modulation classification for linearly modulated signals," *IEEE Trans. Veh. Technol.*, vol. 66, no. 12, pp. 11057–11069, Dec. 2017.

[15] R. Gupta, S. Majhi, and O. A. Dobre, "Design and implementation of a tree-based blind modulation classification algorithm for multiple-antenna systems," *IEEE Trans. Instrum. Meas.*, vol. 68, no. 8, pp. 3020–3031, Aug. 2019.

[16] J. Jin, X. Wu, and Z. Li, "Ultra low power mixer with out-of-band RF energy harvesting for wireless sensor networks applications," *Eng. Rev.*, vol. 40, no. 1, pp. 1–6, 2020.

[17] O. Elsayed, M. Abouzied, V. Vaidya, K. Ravichandran, and E. Sánchez-Sinencio, "An ultralow-power RF wireless receiver with RF blocker energy recycling for IoT applications," *IEEE Trans. Microw. Theory Techn.*, vol. 66, no. 11, pp. 4927–4942, Nov. 2018.

[18] G. H. Tan, R. M. Sidek, and M. M. Isa, "Design of ultra-low voltage and low-power CMOS current bleeding mixer," in *Proc. IEEE Asia–Pac. Conf. Circuits Syst. (APCCAS)*, Ishigaki, Japan, Nov. 2015, pp. 344–347.

[19] M. N. Khormuji, B. M. Popović, and A. G. Perotti, "Enabling SWIPT via OFDM-DC," in *Proc. IEEE Wireless Commun. Netw. Conf. (WCNC)*, Marrakesh, Morocco, Apr. 2019, pp. 1–6.

[20] H. H. Jang, K. W. Choi, and D. I. Kim, "Novel frequency-splitting SWIPT for overcoming amplifier nonlinearity," *IEEE Wireless Commun. Lett.*, vol. 9, no. 6, pp. 826–829, Jun. 2020.

[21] A. G. Perotti, M. N. Khormuji, and B. M. Popović, "Simultaneous wireless information and power transfer by continuous-phase modulation," *IEEE Commun. Lett.*, vol. 24, no. 6, pp. 1294–1298, Jun. 2020.

[22] B. Clerckx, A. Costanzo, A. Georgiadis, and N. B. Carvalho, "Toward 1G mobile power networks: RF, signal, and system designs to make smart objects autonomous," *IEEE Microw. Mag.*, vol. 19, no. 6, pp. 69–82, Sep./Oct. 2018.

[23] J. J. Popoola and R. van Olst, "A novel modulation-sensing method," *IEEE Veh. Technol. Mag.*, vol. 6, no. 3, pp. 60–69, Sep. 2011.

[24] J. Liu and Q. Luo, "A novel modulation classification algorithm based on daubechies5 wavelet and fractional Fourier transform in cognitive radio," in *Proc. IEEE Int. Conf. Commun. Technol. (ICCT)*, Chengdu, China, Nov. 2012, pp. 115–120.

[25] D. Das, A. Anand, P. K. Bora, and R. Bhattacharjee, "Cumulant based automatic modulation classification of QPSK, OQPSK, $\pi/4$-QPSK and 8-PSK in MIMO environment," in *Proc. IEEE Int. Conf. Signal Process. Commun. (SPCOM)*, Bangalore, India, Jun. 2016, pp. 1–5.

[26] U. Satija, M. S. Manikandan, and B. Ramkumar, "Performance study of cyclostationary based digital modulation classification schemes," in *Proc. Int. Conf. Int. Inf. Syst. (ICIIS)*, Gwalior, India, Dec. 2014 pp. 1–5.

[27] A.-B. Salberg and A. Swami, "Doppler and frequency-offset synchronization in wideband OFDM," *IEEE Trans. Wireless Commun.*, vol. 4, no. 6, pp. 2870–2881, Nov. 2005.

[28] R. Gupta and I. Krikidis, "A new receiver design: simultaneous wireless power transfer with modulation classification," in *Proc. IEEE Wireless Power Transfer Conf. (WPTC)*, Seoul, South Korea, 2020, pp. 331–333.

[29] S. Haykin, *Communication Systems*, 4th ed. New York, NY, USA: Wiley, 2001.

[30] S. Pasupathy, "Minimum shift keying: A spectrally efficient modulation," *IEEE Commun. Mag.*, vol. 17, no. 4, pp. 14–22, Jul. 1979.

[31] J. G. Proakis and M. Salehi, *Communication Systems Engineering*, 2nd ed. Upper Saddle River, NJ, USA: Prentice-Hall, 2002.

[32] L. Liu, R. Zhang, and K.-C. Chua, "Wireless information and power transfer: A dynamic power splitting approach," *IEEE Trans. Commun.*, vol. 61, no. 9, pp. 3990–4001, Sep. 2013.

[33] W. Liu, X. Zhou, S. Durrani, and P. Popovski, "SWIPT with practical modulation and RF energy harvesting sensitivity," in *Proc. IEEE Int. Conf. Commun.*, Kuala Lumpur, Malaysia, May 2016, pp. 1–7.

[34] Y. Dong, M. J. Hossain, and J. Cheng, "Performance of wireless powered amplify and forward relaying over Nakagami-*m* fading channels with nonlinear energy harvester," *IEEE Commun. Lett.*, vol. 20, no. 4, pp. 672–675, Apr. 2016.

[35] E. Boshkovska, D. W. K. Ng, N. Zlatanov, and R. Schober, "Practical non-linear energy harvesting model and resource allocation for SWIPT systems," *IEEE Commun. Lett.*, vol. 19, no. 12, pp. 2082–2085, Dec. 2015.

[36] *National Instruments Universal Software Radio Peripheral USRP Platform*, Nat. Instrum. Corp., Austin, TX, USA, 2021. [Online]. Available: http://www.ni.com

[37] *Power Management IC Development Tools*, Powercast Corp., Pittsburgh, PA, USA, 2021. [Online]. Available: https://www.powercastco.com

[38] "MATLAB: Math. Graphics. Programming." The MathWorks, Inc. 2021. [Online]. Available: https://www.mathworks.com/products/matlab.html

[39] *European Digital Cellular Telecommunications System (Phase 2); Physical Layer on the Radio Path; General Description (GSM 05.01)*, Standard SS-ETS 300573, 1996.